

Mean storms: Composites of radar reflectivity images during two decades of severe thunderstorm events

Alex M. Haberlie¹  | Walker S. Ashley² | Marisa R. Karpinski¹

¹Department of Geography and Anthropology, Louisiana State University, Baton Rouge, Louisiana

²Department of Geographic and Atmospheric Sciences, Northern Illinois University, DeKalb, Illinois

Correspondence

Alex M. Haberlie, Department of Geography and Anthropology, Louisiana State University, Baton Rouge, LA 70803. Email: ahaberlie1@lsu.edu

Funding information

Climate Program Office, Grant/Award Number: NA13OAR4310183; Louisiana Board of Regents, Grant/Award Number: LEQSF(2019-22)-RD-A-07; National Science Foundation, Grant/Award Number: ATM-1637225

Abstract

This research quantifies the spatiotemporal statistics of composite radar reflectivity in the vicinity of severe thunderstorm reports. By using over 20 years (1996–2017) of data and 500,000 severe thunderstorm reports, this study presents the most comprehensive analysis of the mesoscale presentation of radar reflectivity composites during severe weather events to date. We first present probability matched mean composites of approximately 5,000 radar images centred on tornado reports that contain one of three types of manually-labelled convective storm modes—namely, (a) quasi-linear convective system (QLCS); (b) cellular; or (c) tropical system. Next, we generate composites for tornado report data stratified by EF-scale and for four temporal periods during which notable severe weather events took place. The data are then stratified by hazard, region, season, and time of day. The results show marked spatiotemporal and intra-hazard variability in radar presentation. In general, cellular convection is favoured in the Great Plains of the United States, whereas QLCS convection is favoured in the Southeast United States. Night and cool-season subsets showed a preference for QLCS convection, whereas day and warm-season subsets showed a preference for cellular convection. These results agree well with the existing literature and suggest that the data extraction and organization approach is sound. Because of this, these data will be useful for future image classification studies in climate and atmospheric sciences—particularly those involving storm mode classification.

KEY WORDS

radar climatology, severe weather, weather radar

1 | INTRODUCTION

Severe thunderstorm events are responsible for many weather-related injuries, deaths, and billion-dollar-losses in the United States (Ashley, 2007; Black and Ashley, 2010; Schoen and Ashley, 2011; Smith and Katz, 2013). Due to their high-impact nature, reports of these events—including when and where they occurred—have been gathered and systematically archived for decades by

organizations like the National Oceanic and Atmospheric Administration's Storm Prediction Center. Examples of how these data are used include storm warning verification (Brooks and Correia Jr., 2018), generating hazard climatologies (Brooks *et al.*, 2003; Allen and Tippett, 2015; Edwards *et al.*, 2018), informing teleconnection relationships (Allen *et al.*, 2015), exploring changes in the spatiotemporal occurrence of events (Brooks *et al.*, 2014; Gensini and Brooks, 2018), vulnerability and exposure

analyses (Strader *et al.*, 2017), and environmental analyses (Thompson *et al.*, 2012). Of particular interest in the field of severe thunderstorm research has been the automated identification of convective storm mode (CSM) in weather radar data through manual (Smith *et al.*, 2012; Ellis *et al.*, 2019) or automated approaches (Haberlie and Ashley, 2018; Gagne II *et al.*, 2019; McGovern *et al.*, 2019; Jergensen *et al.*, 2020).

Weather radar data has been used for decades to identify CSM (e.g., Fujita, 1965). CSM identification can help assess the potential severity of an ongoing or imminent severe weather event (McNulty, 1995; Smith *et al.*, 2012), and can also be a useful tool for assessing operational (Snively and Gallus Jr., 2014) and climate model (Haberlie and Ashley, 2019) performance. The maturation of historical weather radar data archives has allowed the climatological exploration of radar-derived event (e.g., thunderstorms, **CSM**) frequency (Matyas, 2010; Fabry *et al.*, 2017). For example, mean composite frequency of radar-derived events has been used to explore the relationship between locations with significant human-made land use modification and thunderstorm frequency (Ashley *et al.*, 2012; Haberlie *et al.*, 2015). Additionally, the millions of radar images generated and archived since the 1990s have been a great resource for applied machine learning researchers in the atmospheric and climate sciences (McGovern *et al.*, 2019), including projects that train machine learning algorithms to identify **CSM** (e.g., Haberlie and Ashley, 2018; Ashley *et al.*, 2019; Jergensen *et al.*, 2020). However, until now, there has been no attempt to create a curated dataset of radar images centred on classifiable “objects.” These types of datasets are common in the field of machine learning, and are widely used for comparing the efficacy of different approaches. For example, the MNIST dataset (LeCun *et al.*, 1998)—a collection of hand-written numbers—is publically available and has been referenced by tens of thousands of papers. Domain-specific examples include images of galaxies (Lintott *et al.*, 2011) and satellite images centred on tropical systems (Knapp *et al.*, 2016). This work is the first step in communicating the general attributes of this novel dataset which can inform future projects that use these data.

This work seeks to extend the methodology used by “stationary window” radar analyses by instead centring the radar images to be composited on locations and times at which reported thunderstorm hazards occurred. This moving window approach has been used in previous work to assess the influence of multiple cities on thunderstorm activity (Fabry *et al.*, 2017), generate composites of current and future heavy rainfall events (Prein *et al.*, 2017), the successes and failures of machine learning model predictions (McGovern *et al.*, 2019), and the

strengths and weaknesses of various multi-model averaging approaches on modelled rainfall output (Clark, 2017). However, those works used 10s or 100 s of “windows” and did not examine the spatial variability of the composites. This research expands these results to examine composites using over 500,000 radar images from various regions, times of the day, seasons, and event magnitudes. Additionally, it could provide a methodology for communicating morphological variability and evolution within events of interest beyond morphological statistics (Zick and Matyas, 2016; Matyas *et al.*, 2018). Through a moving window composite analysis, we visualize the spatiotemporal patterns in radar reflectivity in the vicinity of severe thunderstorm events in the conterminous United States (**CONUS**). Additionally, we show that the spatial, seasonal, and diurnal composite **CSM** tendencies match with those of existing **CSM** climatologies. This suggests that the dataset created through this work will be useful for machine learning applications, and in particular, **CSM** identification using image classification algorithms (LeCun *et al.*, 1998).

2 | DATA AND METHODS

2.1 | Radar data

This study utilizes historical (1996–2017) national reflectivity composite mosaic ($2 \times \sim 2$ km grid spacing) data called NOWrad_{tm} (The Weather Company). The raw data, which are integers (0–16) representing 5 dBZ bins from 0 to 80 dBZ, are sampled at 15-min intervals and interpolated to a 2×2 km (4 km^2) equal area grid that spans the CONUS in a rectangle from approximately 110–65 W and 25–50 N. These data have been used in a number of climatological studies (Fabry *et al.*, 2017). Although issues exist within radar datasets, some of these are reduced in composite reflectivity by using data from multiple radars (Fabry *et al.*, 2017). We address range- and terrain-based issues by limiting the study area to regions with good low-level radar coverage east of the Rocky Mountains (Figure 1). One important caveat is that dBZ was used in all calculations, and the values were not first converted to Z. Although the literature has argued for both approaches (Lakshmanan, 2012; Warren and Protat, 2019), these differences will not have a large influence on the interpretation of the results.

2.2 | Severe weather event data

The Storm Prediction Center’s severe report dataset was used for event selection (SVRGIS; <http://www.spc.noaa.gov>.

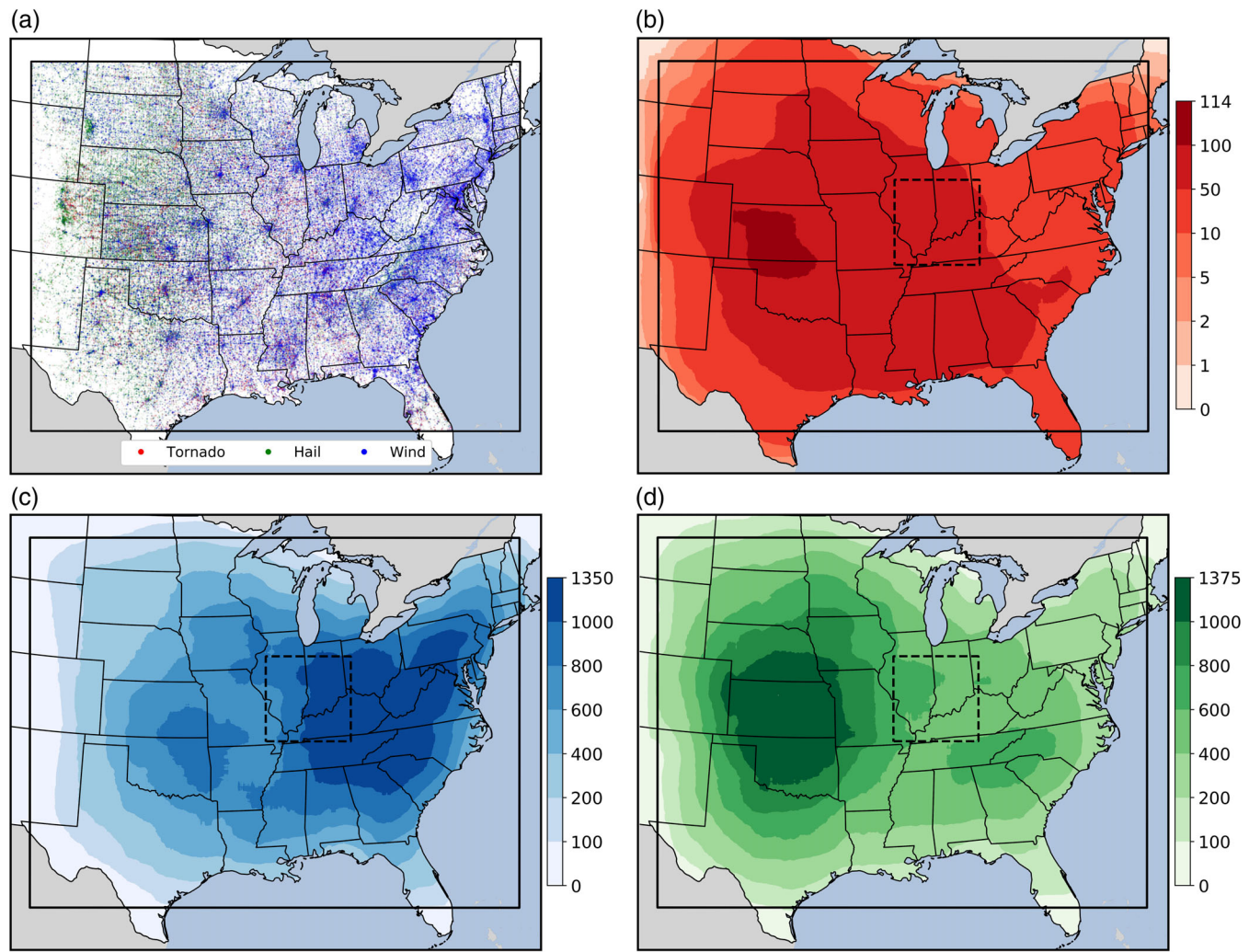


FIGURE 1 Study domain (black outline) and data from 1996 to 2017 for (a) severe weather report locations, and annual mean “report box” frequencies for (b) tornadoes, (c) hail, and (d) wind. The black dashed box in (b-d) represents an example of the extent of a 512 × 512 km “report box” [Colour figure can be viewed at wileyonlinelibrary.com]

gov/gis/svrgis). Although the dataset contains well-known biases (Allen and Tippett, 2015; Edwards *et al.*, 2018), no initial filtering is performed. All reports from 1996 to 2017 are cross-referenced with time-indexed radar reflectivity data to only select event reports that occurred within 7.5 min of available 15-min radar data. An additional step subsets the data within the central and eastern CONUS where event locations are at least 256 km from the edge of the interpolated radar domain (Figure 1). After the filtering process is completed, over 90% of the original severe reports—24,940 tornado, 247,875 hail, and 275,568 wind—are retained. The large sample size, cross-referencing with radar data, and no temporal trend analyses limit the influence of the biases in the dataset. The starting coordinates (e.g., “slat,” “slon”) are used to determine the report’s location.

2.3 | Selection of radar data using filtered SVRGIS reports

For all 548,383 filtered reports, radar data within a 256 by 256 pixel (~512 by ~512 km) box (herein, **report box**) around the report’s converted grid coordinate are extracted and saved (Figure 1b-d). This distance was chosen to represent the mesoscale neighbourhood around each report since all **CSMs** exist within the meso-gamma to lower meso-alpha range (Markowski and Richardson, 2011). To examine the accuracy of the process, bulk radar statistics within 64 km of the report’s grid location were calculated. Over 99% of the events had at least 40 km² (roughly the size of a convective cell; Miller and Mote, 2017) of 40 dBZ or greater pixels in the buffer region. That is, almost all of the filtered reports were near legitimate (i.e., non-noise) dBZ values commonly

associated with deep, moist convective precipitation rates (Parker and Knievel, 2005). These images are used to generate composites.

2.4 | Archetype generation

To examine the attributes of select **CSMs** (Gallus Jr *et al.*, 2008), an initial labelled dataset of 5,156 images was generated, consisting of: (a) quasi-linear convective system, or **QLCS** ($n = 2,330$), (b) Cellular ($n = 2,453$), and (c) Tropical ($n = 373$) examples. To create this dataset, images centred on the starting location of tornado reports from 1996 to 2017 were manually assigned to one of the aforementioned **CSMs**. Although the classifications are subjective, we followed the guidance of previous work (e.g., Gallus Jr *et al.*, 2008; Smith *et al.*, 2012; Ashley *et al.*, 2019; Ellis *et al.*, 2019)—specifically, (a) QLCSs are identified by noting a linear organization of pixels ≥ 40 dBZ (i.e., at least a 3 to 1 length to width ratio) with a length of at least 100 km, (b) Cellular cases are identified by noting a circular organization to the ≥ 40 dBZ pixels in the vicinity of the report, and that contiguous circular region is entirely within a 100×100 km box around the report, and (c) Tropical cases are those that occurred near a HURDAT track (Landsea *et al.*, 2015). The reports were gathered from the Southern United States (i.e., Oklahoma, Texas, Arkansas, Louisiana, Mississippi, Tennessee, Alabama, Florida, Georgia, South Carolina, and North Carolina).

Probability matched mean (PMM) composites (Ebert, 2001) are generated to visualize the tendency of reflectivity shape and intensity across the three CSMs and temporal periods (Figure 2). The probability matched approach is used over a simple mean because of the tendency for the latter approach to “smooth out” the large intensity gradients noted within precipitation rate products (Clark, 2017)—one of which is reflectivity (dBZ). This approach produces more realistic spatial patterns of intensity while preserving the shape of the simple mean. Although this approach has historically been used to assess forecast skill of accumulated precipitation fields (Clark, 2017) and simulated reflectivity factor (Surcel *et al.*, 2014), recent work has used this method to generate representative examples of subsets using many observed radar images (McGovern *et al.*, 2019; Lagerquist *et al.*, 2020). To further illustrate the variability that is captured within the **PMM** composites, we first calculated the sums of the 25th and 75th percentile ranked intensity distributions within each subset. We then stratify these subsets by selecting only those images with a ranked intensity distribution sum less than or equal to (greater than or equal to) the 25th (75th) percentile distribution sums. In this way,

we can visualize the extremes within the subsets, and communicate the morphological variability therein.

To confirm that the PMM composite images are more representative than less complex approaches, we compared them to composite images generated by a simple mean and median using the same radar image subsets. Specifically, we calculated the ranked reflectivity (dBZ) found within the composites (i.e., mean, median, and PMM) and compared those to the median ranked reflectivity for the entire subset (Figure 3). The simple mean composite image produces much broader areas of lower reflectivity values (i.e., < 15 dBZ) and fails to reproduce higher reflectivity values (i.e., > 15 dBZ) compared to any given image within the subset. The median composite image generally produces representative coverage for low reflectivity values, but, like the simple mean, it fails to reproduce higher reflectivity values. Ranked reflectivity from the PMM composite image, however, closely traces the median reflectivity ranks for all CSMs, suggesting it is representative of the intensity distribution one would see within the samples. This is consistent with previous work that demonstrated the advantages of PMM composites over the simple ensemble mean of precipitation accumulation, particularly for higher intensity values (Clark, 2017).

The resulting PMM composites suggest that, for all of the selected tornado reports, the composite generated using affiliated 25th percentile radar images (Figure 2a) resemble Cellular CSM, whereas the composite of 75th percentile images (Figure 2c) resemble QLCS CSM. The ranks for the first 0 dBZ pixel suggests that the median coverage of ≥ 5 dBZ pixels is around 36%, whereas this value is 47% for the 75th percentile distribution and 24% for the 25th percentile distribution (Figure 3a). QLCS samples (Figure 2d,e,f) tend to exhibit an elongated area of higher reflectivity values, and this pattern is consistent for the 25th and the 75th percentile composite images. The median coverage of non-zero pixels for QLCS images is around 42%, and the 25th and 75th percentile coverage are $\sim 33\%$ and $\sim 52\%$, respectively (Figure 3b). On the other hand, Cellular examples (Figure 2g,h,i) show some variability between the 25th percentile images (Figure 2g) and the 75th percentile images (Figure 2i). Namely, there is a marked increase in coverage of non-zero reflectivity values for the 75th percentile images. This is the result of “cell-in-cluster” cases, which contrast the “isolated cellular” examples that comprise the 25th percentile subset. Median, 25th, and 75th percentile coverage of non-zero pixels are approximately 26%, 17%, and 37%, respectively, for Cellular examples (Figure 3c). A noticeable and ubiquitous difference between the QLCS and Cellular composites is the lack of 30 dBZ and greater reflectivity values in the southern two-fifths of the Cellular composite images. This reflects the non-contiguous

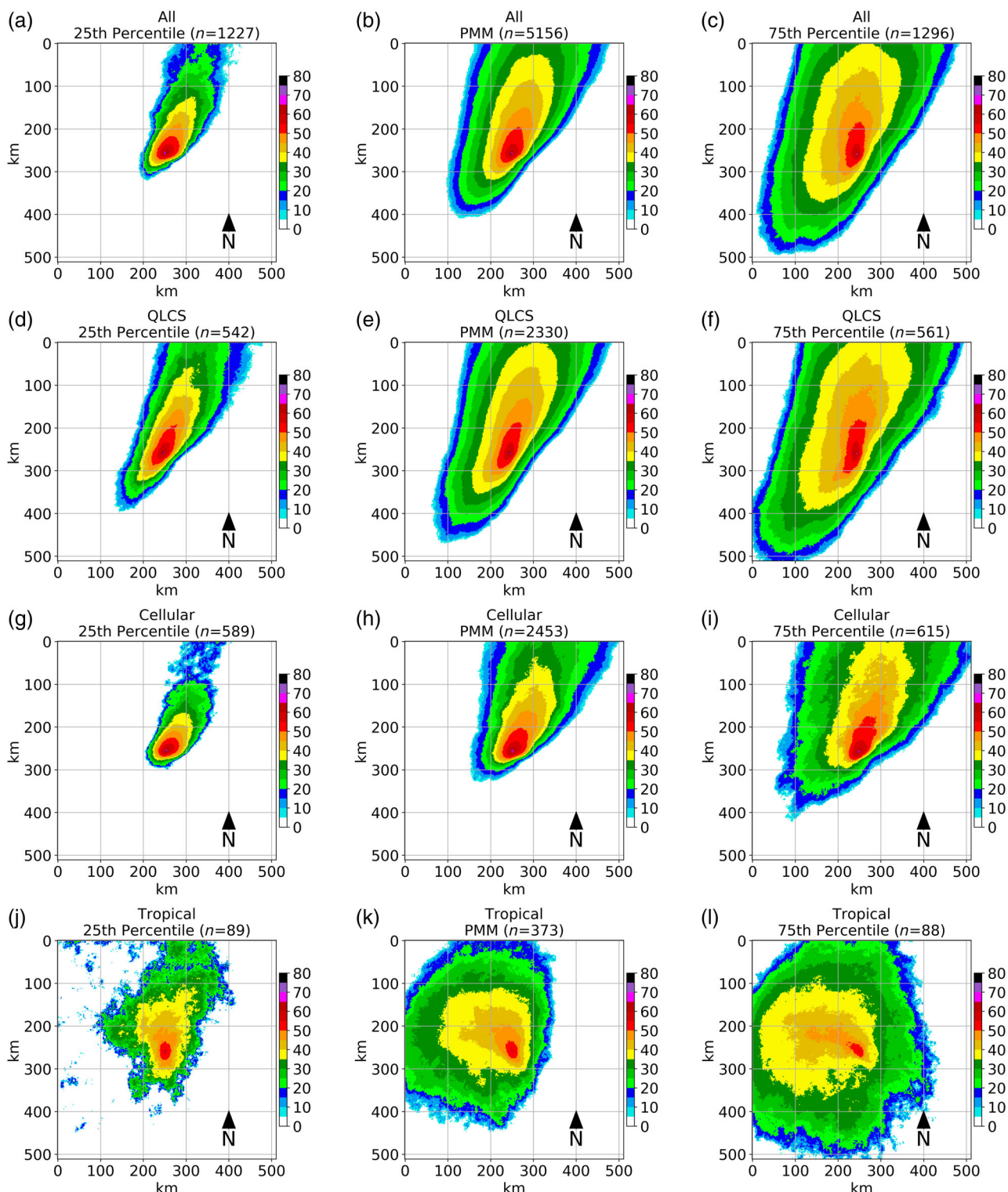


FIGURE 2 Probability matched mean composites calculated using subsets of reflectivity images centred on manually identified tornado (\geq EF1) reports from 1996 to 2017 in the southeast United States organized by convective storm mode. The convective storm modes depicted are (a, b, c) QLCS, cellular, and tropical, (d, e, f) QLCS, (g, h, i) cellular, and (j, k, l) tropical. Three probability matched mean composites were generated from each convective storm mode subset, namely: (a, d, g, j) only images with distribution sums \leq 25th percentile distribution sum, (b, e, h, k) all images, and (c, f, i, l) only images with distribution sums \geq 75th percentile distribution sum [Colour figure can be viewed at wileyonlinelibrary.com]

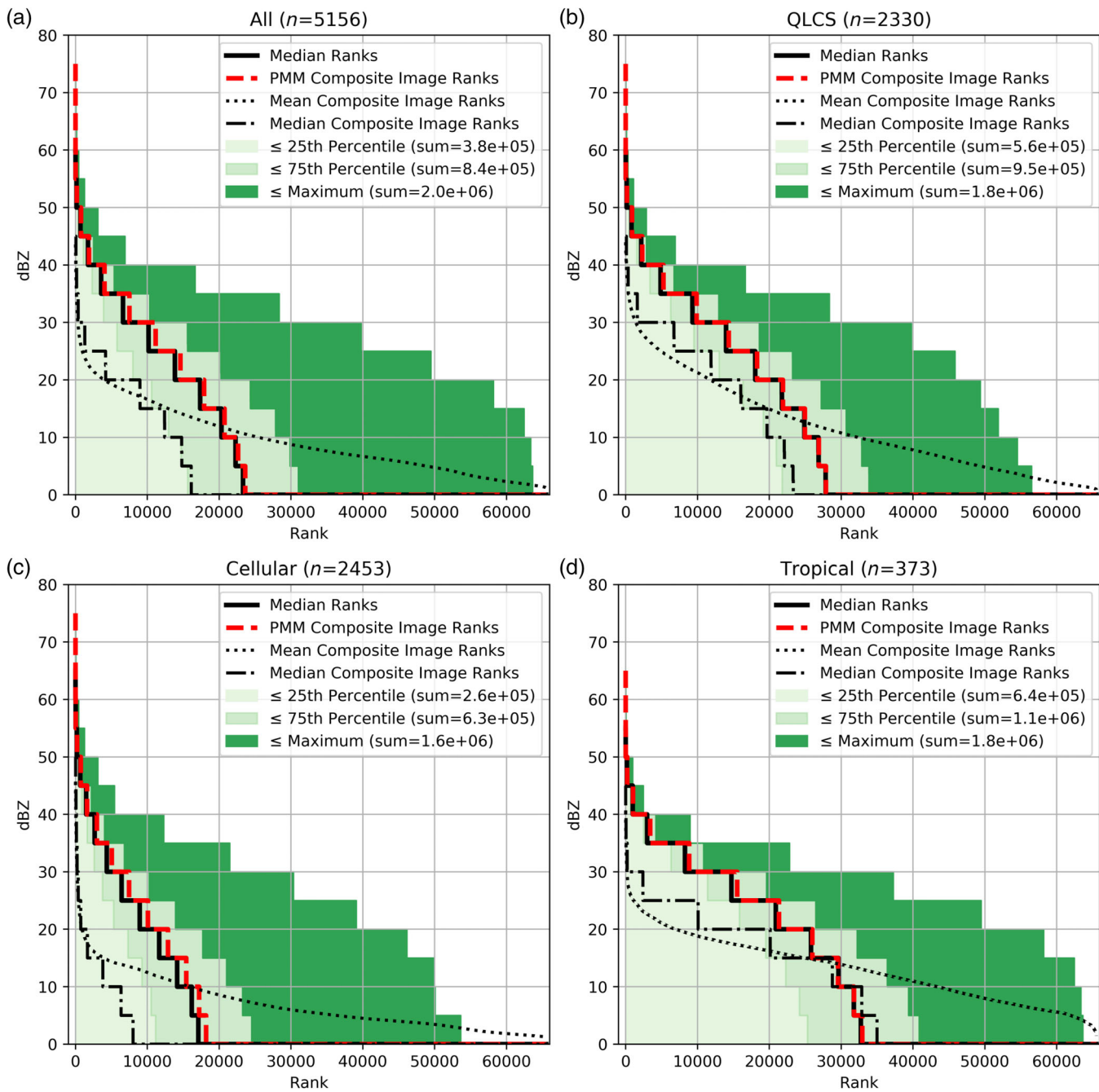


FIGURE 3 Median ranked intensity (black line) in units of dBZ for all images within each convective storm mode subset, namely (a) QLCS, cellular, and tropical, (b) QLCS, (c) cellular, and (d) tropical. For each subset, ranked intensity is also plotted for composite images generated using a probability matched mean (red dashed line), simple mean (black dotted line), and median (black dash-dotted line). The regions representing the $\leq 25^{\text{th}}$ percentile (lightest green), 25th to 75th percentile (medium green), and 75th to maximum (darkest green) distribution regions are colour filled [Colour figure can be viewed at wileyonlinelibrary.com]

nature of “cell-in-cluster” CSM and the preference for tornado formation in “tail-end Charlies,” or supercells that are on the southern flank of a storm cluster (Beveridge *et al.*, 2019). Tropical examples (Figure 2j–l) generally produce more widespread reflectivity values compared to Cellular, but have intensities lower than both QLCS and Cellular samples. Additionally, the

westward offset of lower intensities for Tropical samples, particularly for the overall composite (Figure 2k) and 75th percentile composite (Figure 2l), matches up well with the preferred location of tornadoes relative to the centre of circulation for land falling storms in the CONUS (Edwards, 2012). Median, 25th, and 75th percentile coverage of non-zero pixels for Tropical samples are

approximately 50%, 39%, and 62%, respectively (Figure 3d). Perhaps unsurprisingly, the QLCS/Cellular/Tropical composite depicted in Figure 2b appears as a

combination of the QLCS and Cellular composites (i.e., “mixed mode”), due to their abundance within the manually labelled data. It is also clear that Tropical

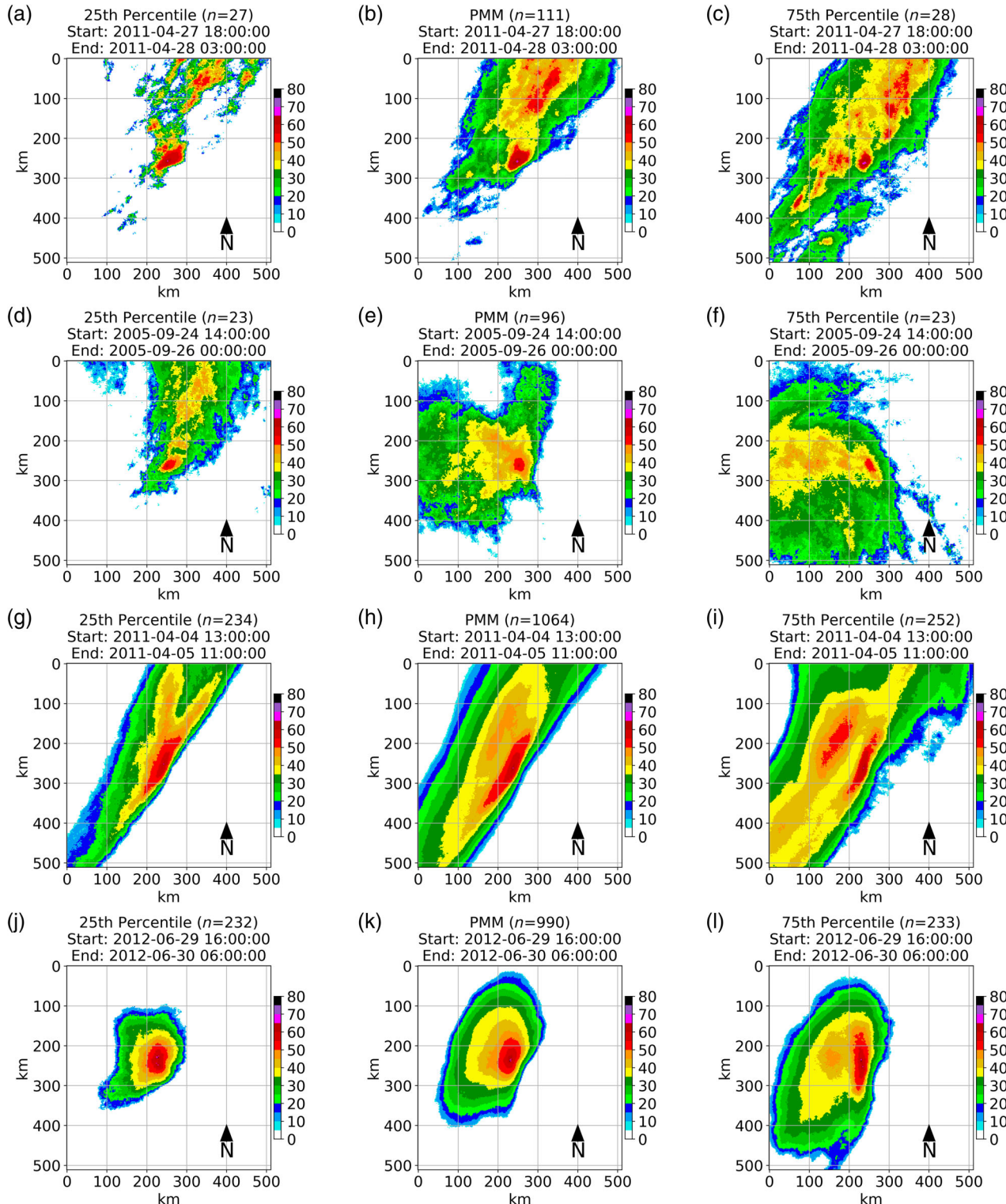


FIGURE 4 As in Figure 2, except for images affiliated with tornado reports from (a, b, c) 1800 UTC on April 27, 2011 to 0300 UTC on April 28, 2011 and (d, e, f) 1400 UTC on September 24, 2005 to 0000 UTC on September 26, 2005 and wind reports from (g, h, i) 1300 UTC on April 4, 2011 to 1100 UTC on April 5, 2011 and (j, k, l) 1600 UTC on June 29, 2012 to 0600 UTC on June 30, 2012 [Colour figure can be viewed at wileyonlinelibrary.com]

samples generally have more non-zero pixels than QLCS and Cellular examples. However, median ≥ 40 dBZ coverage is greater for both QLCS (3.3%) and Cellular (2.2%), compared to Tropical (1.5%). These PMM composite archetypes and statistics are reasonable and can be used to qualitatively assess the CSM tendency within various subsets of unlabelled images.

3 | UNLABELLED IMAGE DATASET

3.1 | Composites from notable events

PMM composite images were generated for tornado reports during notable severe weather events (Figure 4). Specifically, we generated images for the: (a) April 27, 2011 tornado outbreak (Knupp *et al.*, 2014); (b) 24–25 September 2005 Hurricane Rita tornadoes (Moore and Dixon, 2011); (c) 4–5 April 2011 serial derecho event (Corfidi *et al.*, 2016); and (d) June 29, 2012 progressive derecho event (Corfidi *et al.*, 2016). The purpose of these analyses is to further communicate the utility of the composites, as well as identify the variability seen within even the same type of severe weather report. This also provides further verification that the approach is producing reasonable results by affording a qualitative comparison to the radar presentation during these well-documented events.

For the April 27, 2011 event, we focused on the early afternoon to evening period (1800 UTC to 0300 UTC). This period was chosen for demonstration purposes because the predominant storm mode for tornado producing storms was cellular (Knupp *et al.*, 2014), and this tendency is clearly illustrated in Figure 4a–c. Specifically, the pattern shows a strong, high intensity (>50 dBZ), “kidney-bean-shaped” region within 25 km of the center of the image (i.e., the location of the storm reports) in the overall PMM composite (Figure 4b), as well as the 25th (Figure 4a) and 75th percentile (Figure 4c) composites. Additionally, the northern half of the composite has greater coverage of high-intensity pixels, which matches the regional radar depiction during this event. The variability between the 25th and 75th percentile images denote the “isolated cellular” and “cell-in-cluster” events that occurred during this event, and the overall composite reflects these tendencies. Similarly, the composite from the Rita event—where reports were selected from 1400 UTC on September 24, 2005 to 0000 UTC on September 26, 2005—depicts a “bulls-eye” in the center of the image, but with a contrasting northward (Figure 4d) and westward preference (Figure 4e,f) of higher pixel coverage. This pattern represents the preferred location of

tornado reports relative to the center of Rita (Edwards, 2012) and the evolution of this location during the event. Initially, tornadoes were observed in the upper right quadrant of the storm, but this region shifted to the lower right quadrant later in the period. For the wind-report examples, the squall line that produced a serial derecho (Corfidi *et al.*, 2016) is clearly resolved within the 25th percentile (Figure 4g), overall (Figure 4h) and 75th percentile (Figure 4i) composites that include images from 1300 UTC on April 4, 2011 to 0300 UTC on April 5, 2011. Only the central part of the images depicts the classic “quasi-linear” region of high-intensity pixels associated with intense squall lines due to the shifting orientation of the squall line across its ~ 1000 km axis. Similarly, the progressive derecho event of June 29, 2012 (Figure 4j–l) captures the comparatively more compact linear structure and trailing-stratiform precipitation that is typical of the leading-line/trailing-stratiform pattern (Parker and Johnson, 2000). Similar to the Rita event, the stratification by percentile appears to capture the initial cellular structure across the Midwest and the leading-line/trailing-stratiform structure as it moved to the east coast later in its life cycle. Again, Figure 5 illustrates that the PMM approach is more representative of the reflectivity distribution than the mean or median composite images for these events. The April 27th 2011 event (Figure 5a) and the June 2012 derecho both have lower median coverage of non-zero pixels compared to the Rita event (Figure 5b) and the progressive derecho event (Figure 5c). Although there is variability in the orientation, intensity, and location of CSM structures relative to storm reports, tendencies in reflectivity patterns are captured by the composites.

3.2 | Composites stratified by tornado damage rating

Previous work has shown a strong relationship between **CSM** and EF-scale rating (Trapp *et al.*, 2005; Smith *et al.*, 2012; Ashley *et al.*, 2019). Namely, a Cellular CSM is most commonly associated with significant (\geq EF2) to violent (\geq EF4) tornadoes. Thus, composites stratified by EF-scale rating should reflect these findings. For all tornado events considered in this study that were given a rating ($n = 24,850$), their associated images were stratified into groups ranging from EF0 to EF5 (Figure 6; Figure 7). Indeed, the PMM composites show a steady transition from “mixed mode” QLCS and Cellular CSM archetypes (Figure 2) for EF0 to EF2 (Figure 6) to cellular for EF3 and EF4 (Figure 7a–f) to isolated cellular for EF5 (Figure 7g–i). Although there is variability within these composites, there is a clear trend of a reduction in

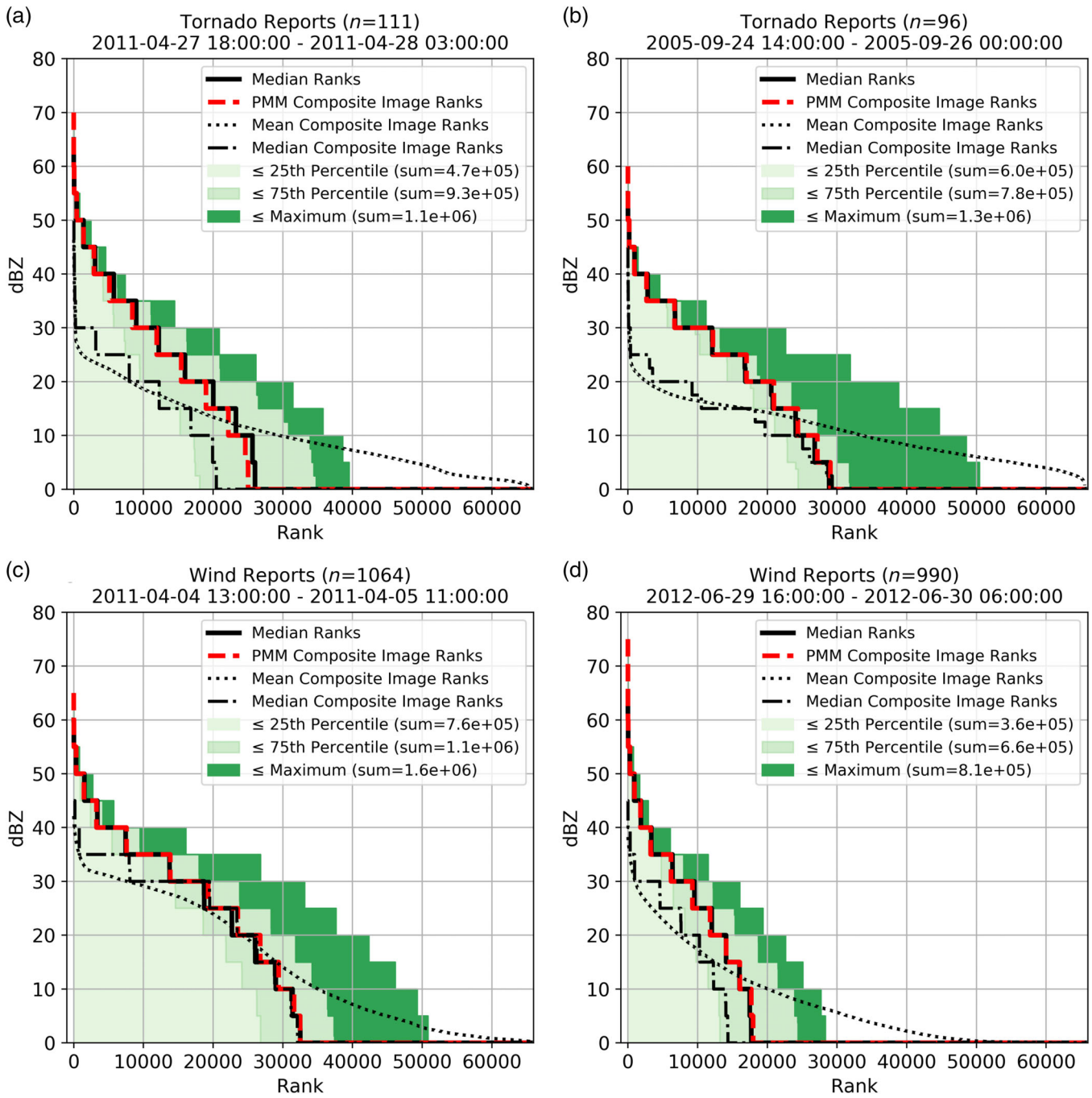


FIGURE 5 As in Figure 3, except for images affiliated with tornado reports from (a) 1800 UTC on April 27, 2011 to 0300 UTC on April 28, 2011 and (b) 1400 UTC on September 24, 2005 to 0000 UTC on September 26, 2005 and wind reports from (c) 1300 UTC on April 4, 2011 to 1100 UTC on April 5, 2011 and (d) 1600 UTC on June 29, 2012 to 0600 UTC on June 30, 2012 [Colour figure can be viewed at wileyonlinelibrary.com]

reflectivity coverage consistent with a shift from QLCS to Cellular CSM as EF-scale rating increases (Figure 8). There is also a marked reduction in the coverage of non-zero pixels in the “maximum” ranked distribution as rating increases. More modest reductions within increasing EF-scale rating are evident in the median, 25th, and 75th percentile non-zero pixel coverage, with

coverage maximizing at EF1 (32%, 21%, and 45%, respectively), and minimizing for EF5s (18%, 12%, and 31%, respectively). Interestingly, however, even the EF3 and EF4 composites have areas of mean convective (≥ 40 dBZ) reflectivity extending to the north, which suggests the possibility of more specific CSMs like those proposed by Smith *et al.* (2012), namely, cell-in-line and cell-in-cluster,

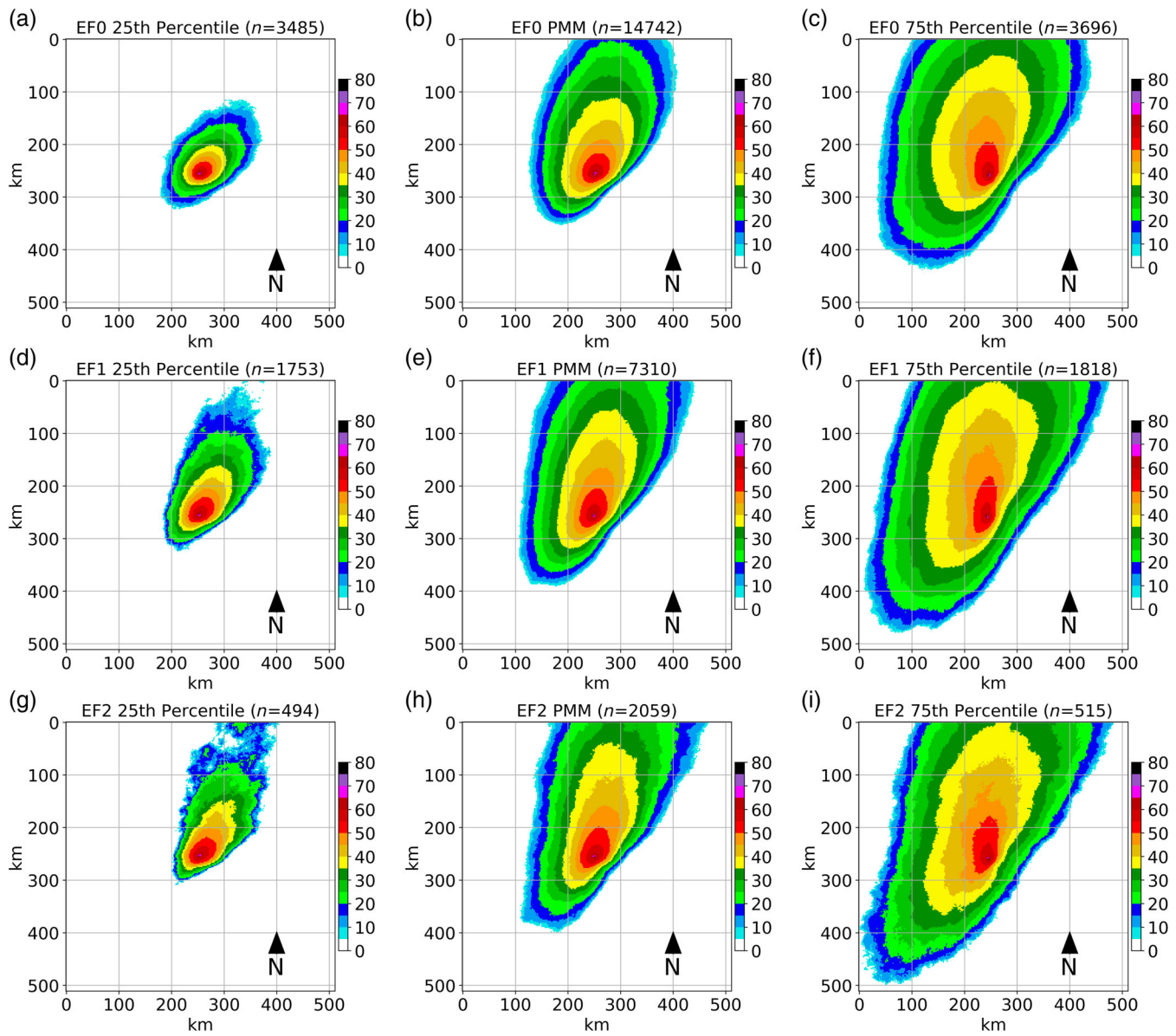


FIGURE 6 As in Figure 2, except for images filtered by EF-scale. Namely, only those images associated with tornadoes rated (a, b, c) EF0, (d, e, f) EF1, and (g, h, i) EF2 [Colour figure can be viewed at wileyonlinelibrary.com]

in addition to QLCS. This “mixed-mode” is illustrated by the differences between the 25th (Figure 6a,d,g; Figure 7a,d) and 75th (Figure 6c,f,i; Figure 7c,f) percentile PMM composite images—specifically, the Cellular CSM in the 25th percentile images and the QLCS/clustered CSM in the 75th percentile images. The CSMs depicted in the 75th percentile images are associated with problematic issues like the highest fatality and injury rate per tornado (supercell in line; Brotzge *et al.*, 2013) and lowest probability of detection (QLCS; Brotzge *et al.*, 2013). These results affirm that even significant to violent tornadoes can occur in “messy” or mixed-mode mesoscale convective scenarios, leading to reductions in warning efficacy.

3.3 | Spatiotemporal variability of composites

To facilitate spatial analyses and comparisons, the eastern CONUS is organized into 29 512×512 km grids and one ocean control grid (Figure 9). Storm reports are associated with a grid using a one-to-one spatial join in *ArcGIS Pro*. Next, **PMM** composites are generated for each grid by only using images associated with reports that occur within that grid (Figure 9). For example, the image plotted within grid 22 (Birmingham) in Figure 9a is the **PMM** composite for all images associated with any severe (tornado, hail, and wind) report that occurred within that grid cell. All of the **PMM** composite images

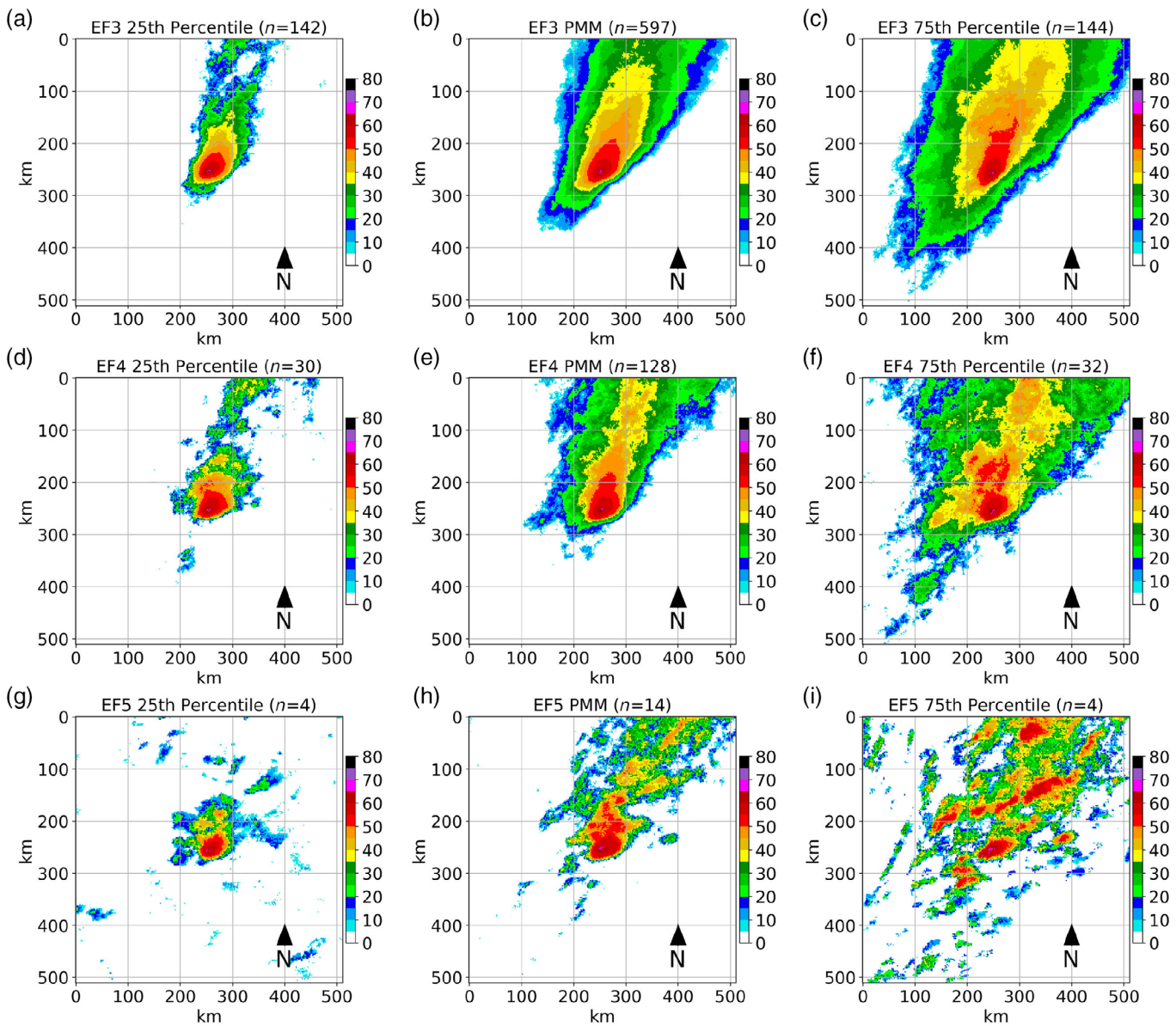


FIGURE 7 As in Figure 2, except for those images associated with tornadoes rated (a, b, c) EF3, (d, e, f) EF4, and (g, h, i) EF5 [Colour figure can be viewed at wileyonlinelibrary.com]

have the same scale as the original data. That is, the **PMM** composite is inserted onto the 2-km equal area grid by anchoring the centre of the image on the pixel closest to the centroid of each grid, and filling out 128 pixels to the north, south, east and west of that central pixel. Through this analysis, we can assess the spatial variability in “typical” radar reflectivity appearance. The colour map used in the composite figures was chosen to replicate the typical colour scale used when presenting weather radar reflectivity. The authors feel that the disadvantages of the generally poor colour map choice are balanced by the familiarity experts and non-experts have with this colour scale.

Marked spatial patterns are illustrated by stratifying the data into gridded regions. The composites for all events (Figure 9a), as well as those stratified by hazard type (Figure 9b-d), show a tendency for radar images to exhibit a more cellular appearance in the High Plains with an increasingly QLCS-like appearance in Southeast CONUS. This pattern is particularly evident within the tornado composites (Figure 9b). Southern Great Plains tornado grids (e.g., 14-Wichita and 20-Dallas) match up well with the cellular archetype depicted in Figure 2g-i, whereas tornado grids within the Southeast CONUS (e.g., 21-Little Rock and 22-Birmingham) match with the QLCS archetype (Figure 2d-f). Conversely, hail

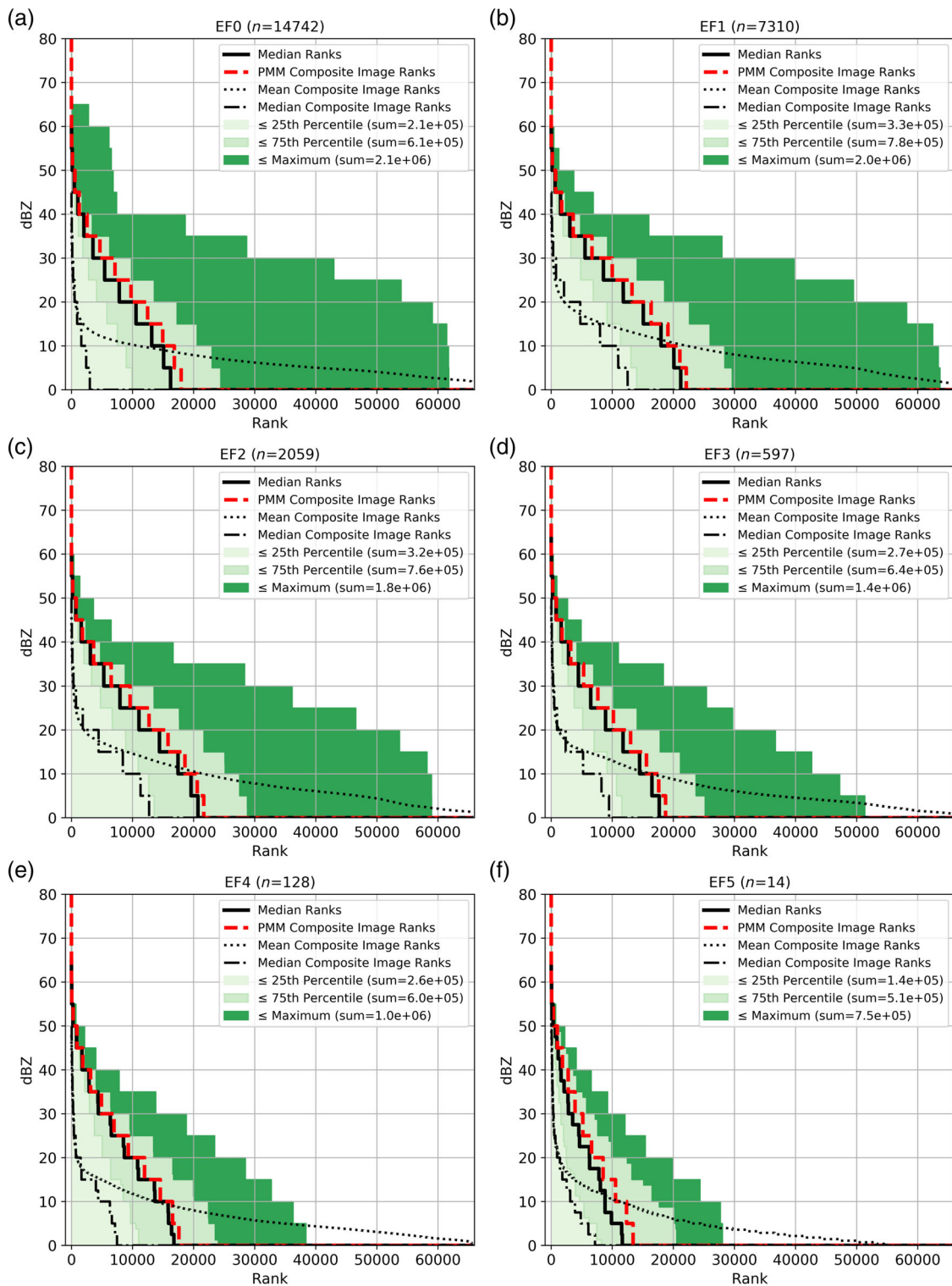


FIGURE 8 As in Figure 3, except for (a) EF0, (b) EF1, (c) EF2, (d) EF3, (e) EF4, and (f) EF5 reports [Colour figure can be viewed at wileyonlinelibrary.com]

composites (Figure 9c) suggest that the preferred storm mode is predominately cellular. Although, the cells appear to be more isolated in grids like 13-Denver compared to 16-Nashville. Wind composites (Figure 9d) show a QLCS-like pattern in the Southeast CONUS, and

a “mixed mode” pattern as depicted in Figure 2b in the Midwest CONUS. The lack of ≥ 5 dBZ to the NW and SE of severe thunderstorm reports is expected and ubiquitous throughout the composites. The initiation and sustenance of deep, moist convection that produces severe

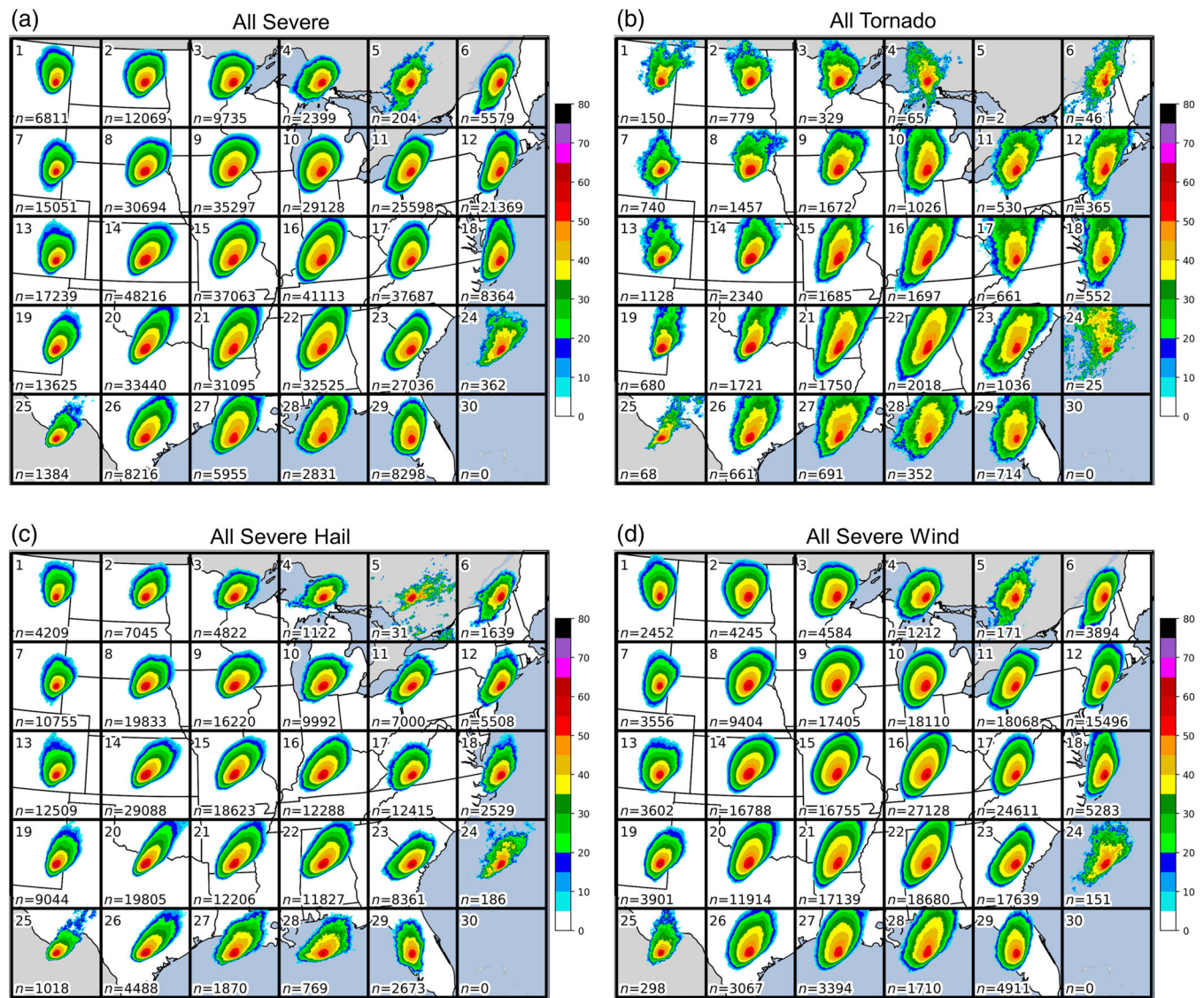


FIGURE 9 As in Figure 2, except for (a) all severe weather events, (b) tornado events, (c) hail events, and (d) wind events from 1996 to 2017 that are spatially filtered by grid (1–30) region. A minimum of 10 reports within a grid was necessary to plot the composites. Each box has the dimensions of 512×512 km [Colour figure can be viewed at wileyonlinelibrary.com]

weather requires a lifting mechanism, which is typically provided by frontal boundaries (McNulty, 1995). To the NW of the report, this is often an area where cold or dry air has undercut warm or moist air, and instability has decreased. To the SE of the report, this area often experiences a capping inversion and air parcels are spatially displaced from an adequate lifting mechanism.

Extending the analysis to warm (April–September) and cool (October–March) seasons reveals temporal variability within the grids (Figure 10). In general, the spatial coverage of the “mean storm” either increases or becomes more elongated during the cool season, particularly for tornado and wind events. Summer tornado events produce composites most similar to the cellular archetype (Figure 2g–i) in the Great Plains and Midwest

CONUS, and an increasing QLCS-like pattern as one moves into the Southeast CONUS (Figure 10a). Focusing on the eastward transition between grids 19–Amarillo, 20–Dallas, 21–Little Rock, and 22–Birmingham, there is a clear evolution from cellular to QLCS-like composites. In contrast, the eastward transition from 7–Casper, 8–Sioux Falls, 9–Des Moines, and 10–Chicago shows a more subtle cellular to QLCS-like transition, potentially caused by more compact QLCSs or a more balanced mix of Cellular and QLCS structures compared to the Southeast. Perhaps not surprisingly, 27–Baton Rouge, 28–Mobile, and 29–Orlando, exhibit a Tropical-like structure in their warm-season tornado composites. These CSMs shift towards QLCS-like structures in the cool season (Figure 10b), and this change is ubiquitous across the

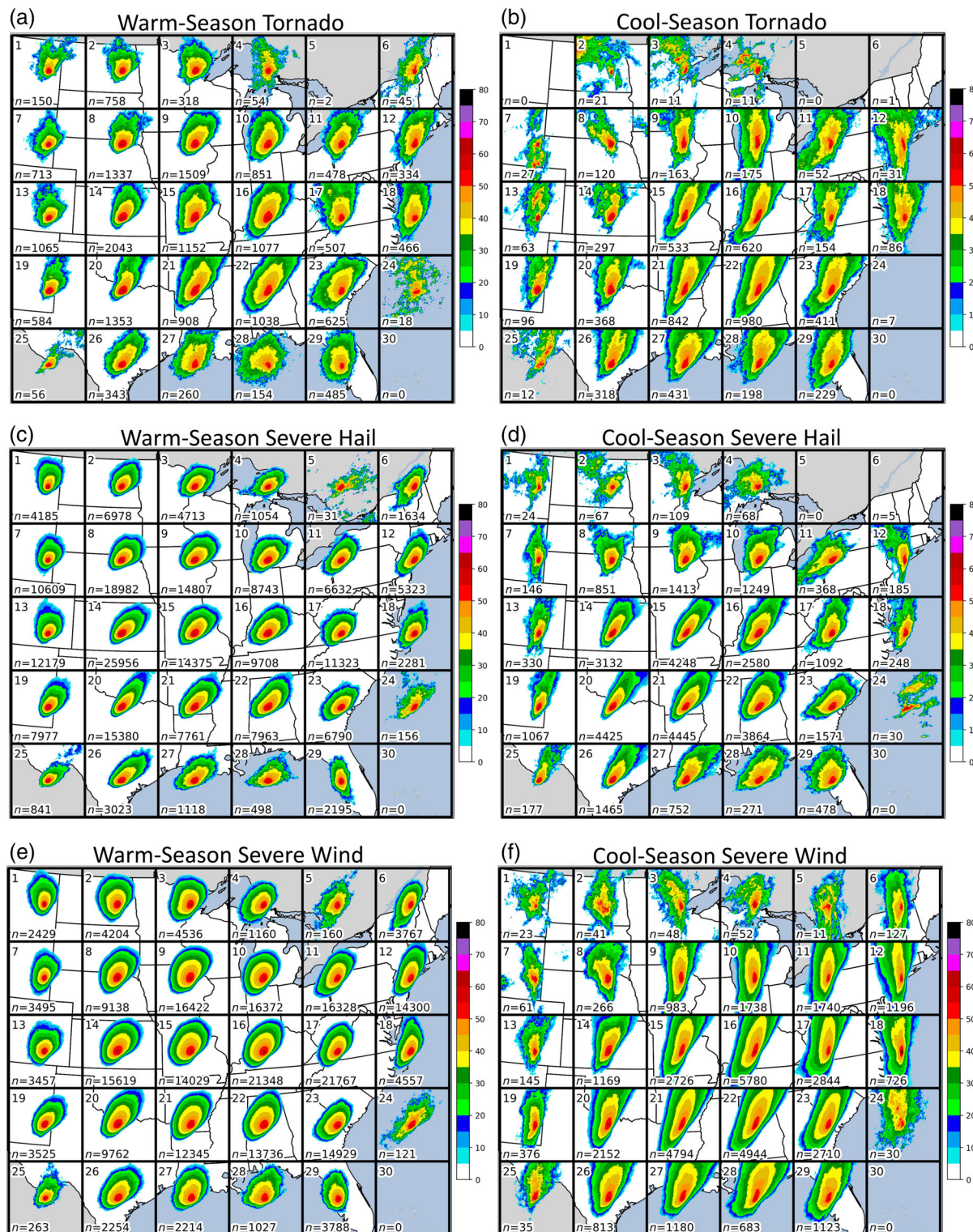


FIGURE 10 As in Figure 9, except for (a, c, e) warm season (April – September), and (b, d, f) cool season (October – March) for all hazard intensities [Colour figure can be viewed at wileyonlinelibrary.com]

grids. This shift is not as obvious for hail events (Figure 10c-d), and although a clear elongation of the spatial coverage of reflectivity intensity is noted, the best qualitative fit for the grids would still be the cellular

archetype in Figure 2g-i. Similar to the tornado composites, the composites for wind events shift from a cellular or mixed-mode pattern in the warm season to a QLCS pattern in the cool season (Figure 10e,f). The seasonal

dichotomy could be explained by a balance between instability and convective inhibition. Convective (≥ 40 dBZ) reflectivity values are often associated with vigorous deep, moist convection (Ashley *et al.*, 2012), and environmental conditions that support such convection have favourable thermodynamics and kinematics (McNulty, 1995). However, the utilization of these ingredients by potential storms is conditioned on other factors such as the strength of a capping inversion and forcing for ascent. During the spring and early summer, a large portion of the study area experiences supportive thermodynamics, kinematics, and conditional environmental factors that lead to the frequent development of widespread convection (Doswell, 2001; Gensini and Ashley, 2011). Moving into the late summer and early fall, stronger capping inversions and weaker forcing can limit the coverage of convection. The result within the composites is the contraction of the “mean storms” due to the limited coverage of non-zero reflectivity values as a response to increasingly localized and less widespread supportive environments during this period.

We stratified the reports into two subsets to examine the influence time of day had on the composites, namely: (a) an early afternoon and early evening subset (1700–0500 UTC); and (b) a night and morning subset (0500–1700 UTC). The limitations of choosing these subsets is that the amount of daylight hours, as well as local noon and local midnight, differs over the course of a year and within the study area. Thus, these periods should be considered only roughly representative of the typical time periods in which initial convection develops (early afternoon and evening) and when upscale growth has occurred (night and morning) based on previous work (Carbone and Tuttle, 2008). Similar patterns to the seasonal analyses emerge from the diurnally-stratified composites (Figure 11). In particular, the transition from the afternoon and evening subset to the night and morning subset results in an increased area covered by the 5 dBZ contour for all of the hazard types and most of the grids. Tornado composites (Figure 11a,b) exhibit a marked expansion in spatial coverage during the night and morning period, including higher intensity contours that denote regions of convection (i.e., 40 dBZ). Some of the more dramatic diurnal increases in reflectivity coverage includes 9-Des Moines and 15-St. Louis. Hail events (Figure 11c,d) experience an expansion in spatial coverage and a change in how the most intense reflectivities are oriented relative to the areas of weaker mean reflectivity during the night and morning period. Specifically, areas of higher intensity are on the southern flank of the 5 dBZ contour region, whereas the afternoon to evening composites have this area on the southwest flank, and this pattern is particularly evident in grids 9-Des Moines

and 10-Chicago. Based on when hail typically occurs in this area (i.e., late spring and early summer), it is possible that this signal is related to the nocturnal low level jet interacting with frontal boundaries (Walters *et al.*, 2008). Wind composites similarly show an expansion of weaker reflectivity (≥ 5 dBZ) and convective reflectivity (≥ 40 dBZ) for many of the grids in the night and morning subsets (Figure 11e,f). This strong signal suggests a preference for QLCS-like structures over cellular structures during this time of the day. Although peak heating occurs during the afternoon, the upscale growth of organized convection associated with severe thunderstorm events is largely relegated to the overnight hours, particularly during the summer (Carbone and Tuttle, 2008; Geerts *et al.*, 2017). The merging and subsequent reinforcement of cold pools as an event matures results in the mesoscale area favourable for lifting parcels to the level of free convection to increase from the meso-gamma scale (~ 10 km) to the meso-beta scale (~ 100 km; Coniglio *et al.*, 2010). Additionally, supportive thermodynamics and kinematics that develop exclusively during the overnight hours allows the development of convection that is displaced from surface frontal boundaries (Walters *et al.*, 2008; Weckwerth *et al.*, 2019). The overall effect of these factors results in the increase in coverage of convection during the overnight and morning period.

4 | DISCUSSION AND CONCLUSIONS

This study used a moving window composite analysis to illustrate the climatological tendency of radar-derived spatial patterns affiliated with recorded severe thunderstorm hazards in the eastern two-thirds of the CONUS. Three CSMs were chosen to illustrate the variability between composites generated for approximately 5,000 manually identified QLCS, Cellular, and Tropical samples. For unlabelled tornado samples, the images were first stratified by F/EF scale to examine the CSM tendency within the resulting composites. To examine the spatiotemporal variability of the composites, over 500,000 images were used to create composites for 30 “report box” grids over the eastern CONUS. This analysis informed an exploration of not only the regional variability of these composites, but also the seasonal and diurnal variability therein.

The results affirm previous work that examined CSM within the CONUS (Smith *et al.*, 2012; Ashley *et al.*, 2019). In particular, strong tornadoes were associated with a “Cellular” CSM tendency, whereas weaker tornadoes were associated with “QLCS” or mixed Cellular/QLCS CSM tendency. CSM tendency within Great

Plains grids was Cellular, whereas the tendency for Southeast CONUS grids was QLCS or mixed Cellular/QLCS. Day and warm-season events preferred a Cellular CSM, whereas cool-season and night events preferred

QLCS or mixed Cellular/QLCS. The results show the utility of the moving window composite approach, due to its agreement with existing manual and automated studies of spatiotemporal CSM variability.

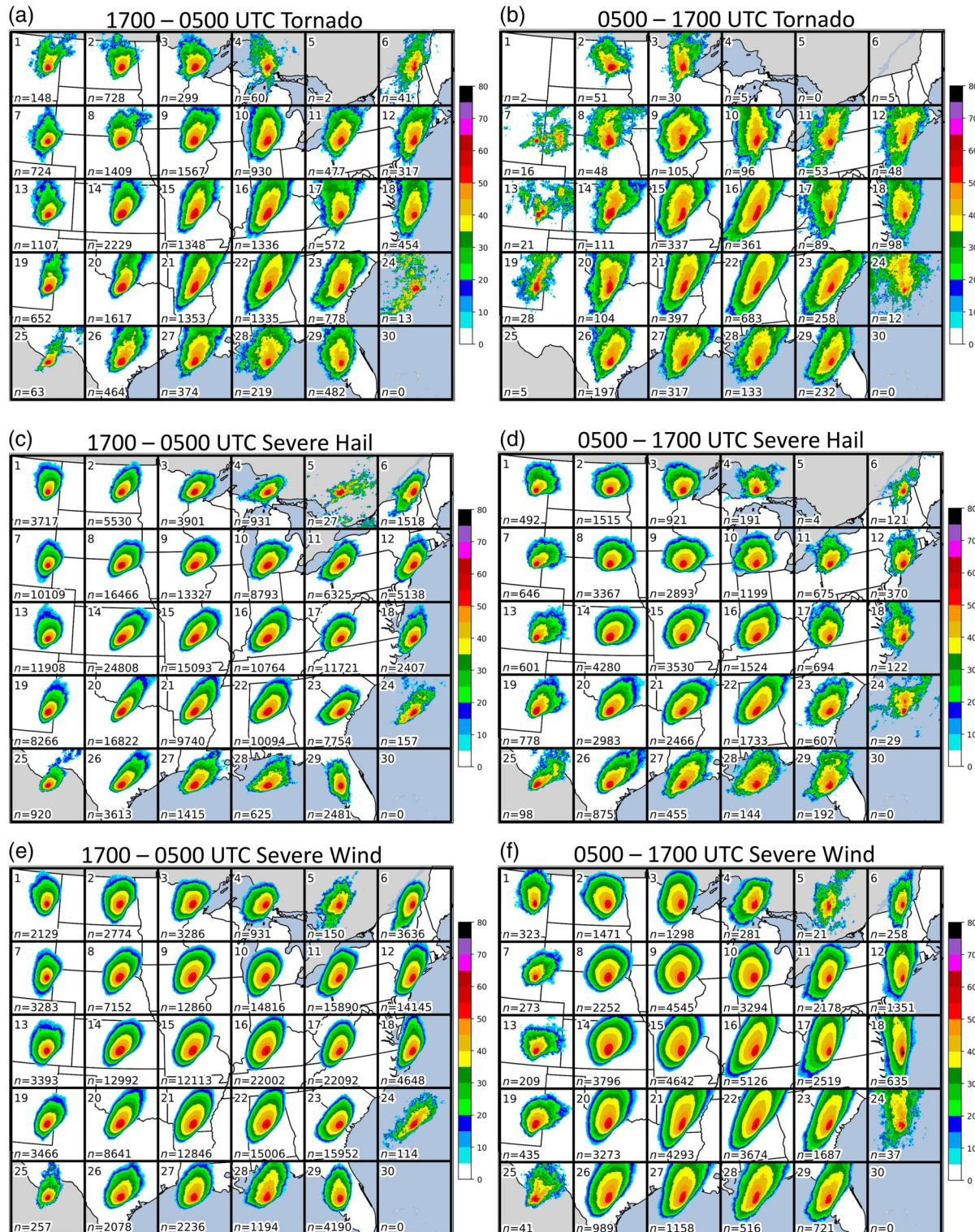


FIGURE 11 As in Figure 9, except for (a, c, e) “afternoon and early evening” (1700–0500 UTC), and (b, d, f) “night and morning” (0500–1700 UTC). For each period, the ending time is not included in that subset [Colour figure can be viewed at wileyonlinelibrary.com]

Future work using these data should explore ways of using semi-supervised (Zhu and Goldberg, 2009) machine learning classification techniques to assign **CSM** labels to the 500,000 extracted images. A large dataset of labelled images would be useful to the meteorology and climate research community, particularly those who are engaged in image classification applications. For example, these data can populate an “image search engine” that can perform image retrieval tasks (Guo *et al.*, 2016). Users of the image search engine would then be able to query the severe weather report dataset by the appearance of the radar image, in addition to the attributes provided within SVRGIS (time, location, magnitude, etc.). Such projects have been successful in other domains (LeCun *et al.*, 1998; Lintott *et al.*, 2011; Knapp *et al.*, 2016) by: (a) providing a consistent dataset from which to draw examples; and (b) adding context to the performance of new machine learning approaches. Additionally, these and similar projects have improved public access to scientific datasets, educated non-experts on physical phenomena, and even included so-called “citizen scientists” in the dataset-building process. Like other projects, this dataset can be modular and add new data as it becomes available through a versioning process.

ACKNOWLEDGEMENTS

This work is supported in part by Louisiana Board of Regents RCS Grant LEQSF(2019-22)-RD-A-07, National Science Foundation Grant ATM-1637225, and NOAA grant NA13OAR4310183. We would like to thank Ryan Lagerquist for the probability matched mean code that helped create the composites. We would also like to thank the two anonymous reviewers for their suggestions that greatly improved the clarity and quality of the paper. Sample analyses and instructions on how to access the data used in this work are available at <https://github.com/ahaberlie/SVRIMG>.

ORCID

Alex M. Haberlie  <https://orcid.org/0000-0001-9172-4028>

REFERENCES

Allen, J.T. and Tippett, M.K. (2015) The characteristics of United States hail reports: 1955-2014. *E-Journal of Severe Storms Meteorology*, 10(3), 1–31.

Allen, J.T., Tippett, M.K. and Sobel, A.H. (2015) Influence of the El Niño/Southern Oscillation on tornado and hail frequency in the United States. *Nature Geoscience*, 8, 278–283.

Ashley, W.S. (2007) Spatial and temporal analysis of tornado fatalities in the United States: 1880-2005. *Weather and Forecasting*, 22, 1214–1228.

Ashley, W.S., Bentley, M.L. and Stallins, J.A. (2012) Urban-induced thunderstorm modification in the Southeast United States. *Climatic Change*, 113, 481–498.

Ashley, W.S., Haberlie, A.M. and Strohm, J. (2019) A climatology of quasi-linear convective systems and their hazards in the United States. *Weather and Forecasting*, 34, 1605–1631.

Beveridge, S.L., Houser, J.L. and Marzola, S.R. (2019) A statistical evaluation of tornado-production tendencies of southernmost supercells compared to adjacent supercells in a north-south-oriented line. *E-Journal of Severe Storms Meteorology*, 14(1), 1–33.

Black, A.W. and Ashley, W.S. (2010) Nontornadic convective wind fatalities in the United States. *Natural Hazards*, 54, 355–366.

Brooks, H.E. and Correia, J., Jr. (2018) Long-term performance metrics for National Weather Service tornado warnings. *Weather and Forecasting*, 33, 1501–1511.

Brooks, H.E., Doswell, C.A., III and Kay, M.P. (2003) Climatological estimates of local daily tornado probability for the United States. *Weather and Forecasting*, 18, 626–640.

Brooks, H.E., Carbin, G.W. and Marsh, P.T. (2014) Increased variability of tornado occurrence in the United States. *Science*, 346, 349–352.

Brotzge, J.A., Nelson, S.E., Thompson, R.L. and Smith, B.T. (2013) Tornado probability of detection and lead time as a function of convective mode and environmental parameters. *Weather and Forecasting*, 28, 1261–1276.

Carbone, R.E. and Tuttle, J.D. (2008) Rainfall occurrence in the US warm season: the diurnal cycle. *Journal of Climate*, 21, 4132–4146.

Clark, A.J. (2017) Generation of ensemble mean precipitation forecasts from convection-allowing ensembles. *Weather and Forecasting*, 32, 1569–1583.

Coniglio, M.C., Hwang, J.Y. and Stensrud, D.J. (2010) Environmental factors in the upscale growth and longevity of MCSs derived from rapid update cycle analyses. *Monthly Weather Review*, 138, 3514–3539.

Corfidi, S.F., Coniglio, M.C., Cohen, A.E. and Mead, C.M. (2016) A proposed revision to the definition of “derecho”. *Bulletin of the American Meteorological Society*, 97, 935–949.

Doswell, C.A. (2001) Severe convective storms—an overview. In: *Severe Convective Storms*. Boston, MA: American Meteorological Society, pp. 1–26.

Ebert, E.E. (2001) Ability of a poor man’s ensemble to predict the probability and distribution of precipitation. *Monthly Weather Review*, 129, 2461–2480.

Edwards, R. (2012) Tropical cyclone tornadoes: a review of knowledge in research and prediction. *E-Journal of Severe Storms Meteorology*, 7, 6.

Edwards, R., Allen, J.T. and Carbin, G.W. (2018) Reliability and climatological impacts of convective wind estimations. *Journal of Applied Meteorology and Climatology*, 57, 1825–1845.

Ellis, K.N., Burow, D., Gassert, K.N., Mason, L.R. and Porter, M.S. (2019) Forecaster perceptions and climatological analysis of the influence of convective mode on tornado climatology and warning success. *Annals of the American Association of Geographers*, 2019, 1–20.

Fabry, F., Meunier, V., Treserras, B.P., Cournoyer, A. and Nelson, B. (2017) On the climatological use of radar data mosaics: possibilities and challenges. *Bulletin of the American Meteorological Society*, 98, 2135–2148.

Fujita, T.T. (1965) Formation and steering mechanisms of tornado cyclones and associated hook echoes. *Monthly Weather Review*, 93, 67–78.

Gagne, D.J., II, Haupt, S.E., Nychka, D.W. and Thompson, G. (2019) Interpretable deep learning for spatial analysis of severe hailstorms. *Monthly Weather Review*, 147, 2827–2845.

Gallus, W.A., Jr., Snook, N.A. and Johnson, E.V. (2008) Spring and summer severe weather reports over the Midwest as a function of convective mode: a preliminary study. *Weather and Forecasting*, 23, 101–113.

Geerts, B., et al. (2017) The 2015 plains elevated convection at night field project. *Bulletin of the American Meteorological Society*, 98, 767–786.

Gensini, V.A. and Ashley, W.S. (2011) Climatology of potentially severe convective environments from the north American regional reanalysis. *E-Journal of Severe Storms Meteorology*, 6 (8), 1–40.

Gensini, V.A. and Brooks, H.E. (2018) Spatial trends in United States tornado frequency. *npj Climate and Atmospheric Science*, 1, 38.

Guo, Y., Liu, Y., Oerlemans, A., Lao, S., Wu, S. and Lew, M.S. (2016) Deep learning for visual understanding: a review. *Neurocomputing*, 187, 27–48.

Haberlie, A.M. and Ashley, W.S. (2018) Identifying mesoscale convective systems in radar mosaics. Part I. Segmentation and classification. *Journal of Applied Meteorology and Climatology*, 57, 1575–1598.

Haberlie, A.M. and Ashley, W.S. (2019) Climatological representation of mesoscale convective systems in a dynamically down-scaled climate simulation. *International Journal of Climatology*, 39, 1144–1153.

Haberlie, A., Ashley, W.S. and Pingel, T. (2015) The effect of urbanization on the climatology of thunderstorm initiation. *Quarterly Journal of the Royal Meteorological Society*, 141, 663–675.

Jergensen, G.E., McGovern, A., Lagerquist, R. and Smith, T. (2020) Classifying convective storms using machine learning. *Weather and Forecasting*, 35(2), 537–559.

Knapp, K.R., Matthews, J.L., Kossin, J.P. and Hennon, C.C. (2016) Identification of tropical cyclone storm types using crowdsourcing. *Monthly Weather Review*, 144, 3783–3798.

Knupp, K.R., et al. (2014) Meteorological overview of the devastating April 27, 2011 tornado outbreak. *Bulletin of the American Meteorological Society*, 95, 1041–1062.

Lagerquist, R., McGovern, A., Homeyer, C. R., Gagne, D. J. and Smith, T. (2020) Deep Learning on Three-dimensional Multi-scale Data for Next-hour Tornado Prediction. *Monthly Weather Review*, 148, 2837–2861.

Lakshmanan, V. (2012) Image processing of weather radar reflectivity data: Should it be done in Z or dBZ. *E-Journal of Severe Storms Meteorology*, 7, 3.

Landsea, C., Franklin, J. and Beven, J. (2015) *The revised Atlantic hurricane database (HURDAT2)*. NOAA/NHC. Available at: <https://www.nhc.noaa.gov>

LeCun, Y., Bottou, L., Bengio, Y. and Haffner, P. (1998) Gradient-based learning applied to document recognition. *Proceedings of the IEEE*, 86, 2278–2324.

Lintott, C., et al. (2011) Galaxy zoo 1: data release of morphological classifications for nearly 900 000 galaxies. *Monthly Notices of the Royal Astronomical Society*, 410, 166–178.

Markowski, P. and Richardson, Y. (2011) *Mesoscale Meteorology in Midlatitudes*. Hoboken, NJ: Wiley-Blackwell.

Matyas, C.J. (2010) Use of ground-based radar for climate-scale studies of weather and rainfall. *Geography Compass*, 4, 1218–1237.

Matyas, C.J., Zick, S.E. and Tang, J. (2018) Using an object-based approach to quantify the spatial structure of reflectivity regions in hurricane Isabel (2003). Part I: comparisons between radar observations and model simulations. *Monthly Weather Review*, 146, 1319–1340.

McGovern, A., Lagerquist, R., Gagne, D.J., Jergensen, G.E., Elmore, K.L., Homeyer, C.R. and Smith, T. (2019) Making the black box more transparent: understanding the physical implications of machine learning. *Bulletin of the American Meteorological Society*, 100, 2175–2199.

McNulty, R.P. (1995) Severe and convective weather: a central region forecasting challenge. *Weather and Forecasting*, 10, 187–202.

Miller, P.W. and Mote, T.L. (2017) Standardizing the definition of a “pulse” thunderstorm. *Bulletin of the American Meteorological Society*, 98, 905–913.

Moore, T.W. and Dixon, R.W. (2011) Climatology of tornadoes associated with Gulf Coast-landfalling hurricanes. *Geographical Review*, 101, 371–395.

Parker, M.D. and Johnson, R.H. (2000) Organizational modes of midlatitude mesoscale convective systems. *Monthly Weather Review*, 128, 3413–3436.

Parker, M.D. and Knievel, J.C. (2005) Do meteorologists suppress thunderstorms?: radar-derived statistics and the behavior of moist convection. *Bulletin of the American Meteorological Society*, 86, 341–358.

Prein, A.F., Liu, C., Ikeda, K., Bullock, R., Rasmussen, R.M., Holland, G.J. and Clark, M. (2017) Simulating north American mesoscale convective systems with a convection-permitting climate model. *Climate Dynamics*, 2017, 1–16.

Schoen, J. and Ashley, W.S. (2011) A climatology of fatal convective wind events by storm type. *Weather and Forecasting*, 26, 109–121.

Smith, A.B. and Katz, R.W. (2013) US billion-dollar weather and climate disasters: data sources, trends, accuracy and biases. *Natural Hazards*, 67, 387–410.

Smith, B.T., Thompson, R.L., Grams, J.S., Broyles, C. and Brooks, H.E. (2012) Convective modes for significant severe thunderstorms in the contiguous United States. Part I: storm classification and climatology. *Weather and Forecasting*, 27, 1114–1135.

Snively, D.V. and Gallus, W.A., Jr. (2014) Prediction of convective morphology in near-cloud-permitting WRF model simulations. *Weather and Forecasting*, 29, 130–149.

Strader, S.M., Ashley, W.S., Pingel, T.J. and Krmenev, A.J. (2017) Observed and projected changes in United States tornado exposure. *Weather, Climate, and Society*, 9, 109–123.

Surcel, M., Zawadzki, I. and Yau, M.K. (2014) On the filtering properties of ensemble averaging for storm-scale precipitation forecasts. *Monthly Weather Review*, 142, 1093–1105.

Thompson, R.L., Smith, B.T., Grams, J.S., Dean, A.R. and Broyles, C. (2012) Convective modes for significant severe thunderstorms in the contiguous United States. Part II: supercell and QLCS tornado environments. *Weather and Forecasting*, 27, 1136–1154.

Trapp, R.J., Tessendorf, S.A., Godfrey, E.S. and Brooks, H.E. (2005) Tornadoes from squall lines and bow echoes. Part I: climatological distribution. *Weather and Forecasting*, 20, 23–34.

Walters, C.K., Winkler, J.A., Shadbolt, R.P., van Ravensway, J. and Bierly, G.D. (2008) A long-term climatology of southerly

and northerly low-level jets for the Central United States. *Annals of the Association of American Geographers*, 98, 521–552.

Warren, R. A. and Protat, A. (2012) Should Interpolation of Radar Reflectivity be Performed in Z or dB Z?. *Journal of Atmospheric and Oceanic Technology*, 36, 1143–1156.

Weckwerth, T.M., Hanesiak, J., Wilson, J.W., Trier, S.B., Degelia, S.K., Gallus, W.A., Jr., Roberts, R.D. and Wang, X. (2019) Nocturnal convection initiation during PECAN 2015. *Bulletin of the American Meteorological Society*, 100, 2223–2239.

Zhu, X. and Goldberg, A.B. (2009) *Synthesis Lectures on Artificial Intelligence and Machine Learning: Introduction to Semi-supervised Learning*. Williston, VT: Morgan and Claypool Publishers.

Zick, S.E. and Matyas, C.J. (2016) A shape metric methodology for studying the evolving geometries of synoptic-scale precipitation patterns in tropical cyclones. *Annals of the American Association of Geographers*, 106, 1217–1235.

How to cite this article: Haberlie AM, Ashley WS, Karpinski MR. Mean storms: Composites of radar reflectivity images during two decades of severe thunderstorm events. *Int J Climatol*. 2020;1–19. <https://doi.org/10.1002/joc.6804>